International Journal of Plasticity 77 (2016) 75–89

Contents lists available at ScienceDirect

International Journal of Plasticity

journal homepage: www.elsevier.com/locate/ijplas

Continuous description of the atomic structure of grain boundaries using dislocation and generalized-disclination density fields

Xiao-Yu Sun [a, *], Vincent Taupin [b], Claude Fressengeas [b], Patrick Cordier [a]

[a] Unité Matériaux et Transformations, UMR 8207 CNRS/Université Lille1, 59655 Villeneuve d'Ascq, France
[b] Laboratoire d'Etude des Microstructures et de Mécanique des Matériaux (LEM3), Université de Lorraine/CNRS, Ile du Saulcy, 57045 Metz Cedex, France

ARTICLE INFO

Article history:
Received 14 July 2015
Received in revised form 30 September 2015
Available online 23 October 2015

Keywords:
A. Grain boundaries
A. Dislocations
Generalized-disclinations
C. Finite differences

ABSTRACT

An atomistic-to-continuum method is developed to derive dislocation, generalized-disclination density fields and the associated elastic strain, rotation, curvature and second-distortion fields from the atomic structure of grain boundaries. From the relaxed and un-relaxed atomic positions, calculation of the transformation gradient feeds a mechanical framework, where discontinuities of the lattice elastic displacement and distortion (rotation and strain) are captured by smooth incompatible strain and second-distortion fields associated with the dislocation and generalized-disclination density fields, respectively. The method is applied to a copper symmetrical tilt boundary as obtained from molecular dynamics simulations. The core structure of the boundary is found to contain edge dislocations and dipoles of generalized-disclinations, including standard wedge-disclination dipoles. The latter reflect in particular localized shear and stretch discontinuities across the interface, in addition to the overall rotation discontinuity.

1. Introduction

In crystalline solids such as rocks or metals, grain boundaries (GBs) are thin material layers where the lattice rotates from one orientation to the next one within a few nanometers. Because they treat these layers as infinitely thin interfaces, large-scale polycrystalline representations fail to describe their structure. Conversely, atomistic representations provide a detailed description of the GBs, but their character remains discrete and not prone to coarse-graining procedures. Continuum descriptions based on kinematic and crystal defect fields defined at interatomic scale are appealing because they can provide smooth and thorough descriptions of GBs, recovering in some sense the atomistic description and potentially serving as a basis for coarse-grained polycrystalline representations. As the elastic properties and mechanical response of GBs (*e.g.*, excess energy, interactions with dislocations) strongly depend on their atomic structure (Tschopp et al., 2008), a major challenge in the development of such continuum descriptions lies in maintaining the essential features of this structure at similar resolution length scale.

* Corresponding author. Université Lille 1, Unité Matériaux et Transformations, UMR CNRS 8207, Bat C6, 59655 Villeneuve d'Ascq Cedex, France. Tel.: +33 320 434341.
E-mail address: xiaoyu.sun@univ-lille1.fr (X.-Y. Sun).

http://dx.doi.org/10.1016/j.ijplas.2015.10.003

The geometrical phase analysis (GPA) is a powerful measurement tool enabling to access continuous deformation fields from high resolution transmission electron microscopy (HRTEM) images of atomic structures (Hÿtch et al., 1998). It provides displacement fields at a spatial resolution below interatomic scale by combining Fourier-space and real-space information and has already been successfully used to analyze a number of defect atomic structures. For instance, the elastic displacement fields around an edge dislocation in silicon were measured with an accuracy of 0.03 Å (Hÿtch et al., 2003). The strain fields around a dislocation in a grain boundary in germanium (Hÿtch et al., 2006) and the structural information on a triple junction in palladium (Rösner et al., 2011) were obtained quantitatively from lattice images. By performing GPA, it is thus possible to uncover a measure of the elastic fields characterizing the core atomic structures of defects.

However, the interpretation of HRTEM images may be difficult because the images sensitively depend on various parameters such as the thickness and composition of the specimen, surface contamination and specimen damage due to ion milling (Rouvière and Sarigiannidou, 2005). Complementary to the GPA method, atomistic simulation results may also be used as an input to derive continuous deformation fields by estimating metric quantities such as the deformation gradient, which can link the discrete atomic structure information to continuum mechanics theories (Zimmerman et al., 2009). Based on this crossover method, the kinematic metrics of continuum mechanics were formulated with atomistic data and leveraged a mechanical field interpretation of the deformation mechanisms governing the plasticity of nanocrystalline materials (Tucker et al., 2010, 2012; Berbenni et al., 2013; Tucker and Foiles, 2015; Prieto-Depedro et al., 2015). However, all these methods stop short of uncovering the hidden incompatibility of the kinematics and the associated defect density field.

Within a recent elasto-plastic framework (Fressengeas et al., 2011), it was proposed that dislocation and dipolar disclination density fields could be the appropriate objects for the continuum mechanics description of the atomic structure of grain boundaries (Fressengeas et al., 2014). Dislocation (respectively disclination) densities render in a continuous fashion the discontinuities of the elastic displacement (respectively rotation) of the crystal lattice in the interface area. They are associated with smooth incompatible, *i.e.* non curl-free, elastic strain (respectively curvature) fields. In the particular case of symmetrical tilt boundaries in copper, it was proposed, based on geometrical considerations, that dipoles of wedge disclination densities could be substituted for the atomic structural units composing the interfaces (Sutton and Vitek, 1983; Tschopp et al., 2008). In doing so, realistic predictions of the influence of GB misorientation on their excess energy (Fressengeas et al., 2014) and shear-coupled migration behavior (Taupin et al., 2014) were obtained. Moreover, it was recently shown that such defect density fields were also appropriate objects to describe tilt GBs in olivine (Cordier et al., 2014) and fullerene mono-molecular layers (Bozhko et al., 2014). Such results are a motivation for the development of a more general method performing the crossover atomistic/continuum by defining unambiguously the crystal defect density fields associated with a given interfacial atomistic structure.

In this paper, we present a computational crossover method that derives (i), kinematic fields showing continuity at interatomic scale from the atomic structure of GBs and (ii), crystal defect density fields from the incompatibility of these fields. To derive smooth kinematic fields, molecular dynamics simulations of grain boundary structures will be used, which does not preclude employing experimental images obtained from high-resolution TEM investigations. A symmetrical tilt boundary in copper will be considered as a benchmark in this paper. Then, in a way that is very similar to recent methods (Gullett et al., 2008; Zimmerman et al., 2009), and will be compared to them, differences in the atomic positions between low-energy relaxed and un-relaxed initial grain boundary configurations will be used to derive the transformation gradient, from which the distortion (strain and rotation) and second-order distortion fields will be derived. Beyond the dislocation/disclination framework of Fressengeas et al. (2011), the definition of the appropriate crystal defect density fields then relies on a recent field dislocation and generalized-disclination framework (Acharya and Fressengeas, 2012). The dislocation density tensor field (Nye, 1953) arises from discontinuities of the elastic displacement and is associated with the incompatible (non integrable or non-holonomic) part of the elastic strain tensor (Kröner, 1980). Similarly, a generalized-disclination density field (Acharya and Fressengeas, 2012) reflects discontinuities of the elastic distortion (strain and rotation) and is related to the incompatible part of the elastic second-order distortion tensor, *i.e.*, the gradient of the elastic distortion in a compatible body without distortion discontinuities. Generalized-disclinations reduce to standard disclinations (deWit, 1970; Fressengeas et al., 2011) when the elastic strain is continuous and only rotation discontinuities exist. They complement standard disclinations by accounting for possible discontinuities of shear and stretch in addition to rotation discontinuities.

The outline of the paper is as follows. In section 2, the molecular dynamics simulation of a copper [100] symmetrical tilt boundary of misorientation 18.9° is presented. In section 3, the computational method used to calculate the transformation gradient, distortion and second-order distortion fields from atomic configurations, is derived. In section 4, the dislocation and generalized-disclination field theoretical framework is briefly recalled. The kinematic and crystal defect density fields obtained for the copper tilt boundary are presented and analyzed in section 5. Conclusions follow.

2. Molecular dynamics simulations of the grain boundary structure

As shown in Fig. 1, the simulated grain boundary is a copper Σ37 (610)[100] symmetrical tilt boundary of misorientation $\theta = 18.9°$, which was recently modeled by using dipoles of wedge disclination densities (Fressengeas et al., 2014). As such, the defect densities and the associated kinematic fields will be compared to those obtained in the present paper. In the work of Fressengeas et al. (2014), the continuous disclination description of the boundary was built by using a top-down approach through geometrical assumptions, while in the present work, the dislocation and disclination densities in grain boundary are

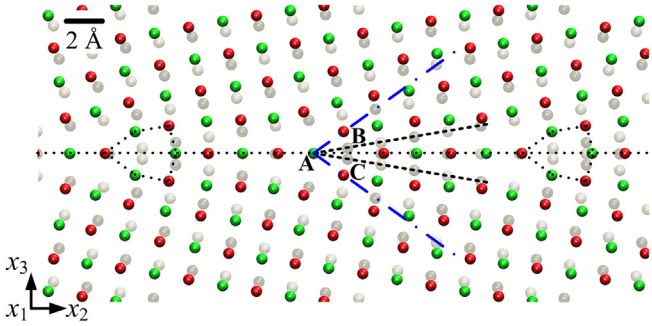

Fig. 1. Reference low-energy relaxed configuration (colored) and current high-energy un-relaxed configuration (black and white) of the copper Σ37 (610)[100] symmetrical tilt boundary, as obtained from molecular dynamics simulations. Black/white or red/green balls correspond to atoms belonging to two consecutive atomic planes parallel to the figure in both crystals. The coordinate axis system used for field calculations is shown on the bottom left corner. (For interpretation of the references to color in this figure legend, the reader is referred to the web version of this article.)

computed with no *a priori* from atomistic structures with atomic positions from molecular dynamics simulation. Thus, the continuous description of the boundary is built by a "bottom-up" processing.

To generate this tilt boundary, we follow standard methods. Two adjacent copper crystals are first separately rotated symmetrically about the [100] axis, the lower one by an angle $-\theta/2$ and the upper one by an angle $+\theta/2$. Then, the extremities of both grains are cut and joined together with respect to coincidence site lattice points to form an initial un-relaxed bicrystal configuration. In the process, atoms may be added or removed in the grain boundary area to minimize crystal incompatibility. In particular, it is carefully checked that there is no missing atom or atom overlapping. This initial bicrystal is a high-energy configuration that needs to self-relax by rearrangement of the atomic positions. To simulate such relaxation, we performed molecular dynamics simulations.

The program Atomsk (Hirel, 2015) and simulation code LAMMPS (Plimpton, 1995) were used. We used the empirical embedded-atoms method (EAM) interatomic potential developed by Mishin et al. (2001) and calibrated with respect to *ab-initio* values of twin and stacking fault energies. The grain boundary energy is relaxed to its minimum energy configuration by using the conjugate gradient method and then thermally equilibrated for 60 ps by using a Nosé-Hoover thermostat (Martyna et al., 1994). To avoid thermal noise in the case of higher temperature, we used a temperature of 1 K. The final low-energy relaxed configuration is shown in Fig. 1. It was checked that this configuration is the lowest energy configuration among other possible structures by relaxing different initial configurations. In particular, we swept the interval of in plane relative translations of the initial crystals along the direction perpendicular to the rotation axis. The lowest energy configuration shown in Fig. 1 is thus used in the following for the calculation of kinematic and defect density fields.

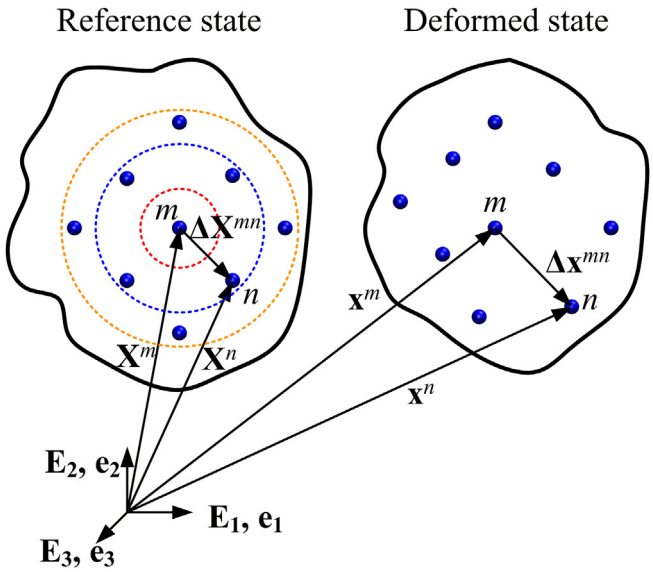

Fig. 2. Illustration of the transformation gradient associated with the motion of material particles from the reference state to the current state.

3. Crossover from atomistic to continuum

3.1. Transformation gradient

In continuum mechanics, the calculation of the transformation gradient requires the knowledge of a reference (R) and a current (C) configuration. If the vector **X** denotes the position of a material point in a body with respect to a reference coordinate system and the vector **x** provides the new position in the current configuration, the transformation gradient writes

$$\mathbf{F} = \frac{\partial \mathbf{x}}{\partial \mathbf{X}}; \quad \mathrm{F}_{ij} = \partial \mathrm{x}_i / \partial \mathrm{X}_j. \tag{1}$$

In the case of the grain boundary presented above, the reference configuration is chosen to be the low-energy relaxed structure (colored atoms in Fig. 1) and the current configuration is the initial un-relaxed configuration (black and white atoms in Fig. 1). In the grain boundary relaxation process, all atoms of the lattice keep their neighbors. Therefore, their displacements are elastic, and the transformation gradient, distortion (strain, rotation), and second-distortion fields to be derived from these displacements in the following are elastic fields. The transformation gradient field associated with the current and reference atomic configurations is calculated by the following procedure. As sketched in Fig. 2, an atom m is located at a position $\mathbf{X^m}$ in the reference configuration. It moves to the new position $\mathbf{x^m}$ in the current configuration. The relative position of a neighboring atom n with respect to atom m is given by the finite difference

$$\mathbf{\Delta X^{mn}} = \mathbf{X^n} - \mathbf{X^m} \tag{2}$$

in the reference configuration and by

$$\mathbf{\Delta x^{mn}} = \mathbf{x^n} - \mathbf{x^m} \tag{3}$$

in the deformed configuration. The component of the transformation gradient at atom m induced by the variation of the relative position of atom n is then approximated by

$$F_{ij}^{\mathrm{mn}} \approx \frac{\Delta x_i^{\mathrm{mn}}}{\Delta X_j^{\mathrm{mn}}}. \tag{4}$$

Since there is more than one neighboring atom near atom m, the component of transformation gradient at the atom location is averaged over all neighboring atoms n:

$$F_{ij}^{m} = \frac{1}{N} \sum_{\left(r_{mn} \le r_{\mathrm{cutoff}}\right)} \mathrm{F}_{ij}^{mn}, \tag{5}$$

where r_{mn} is the distance between atoms m and n in the reference configuration, r_{cutoff} is a cut-off distance introduced to consider whether or not an atom n is in the neighborhood of atom m, and N is the total number of neighboring atoms identified within the cut-off distance. It is clear that the cut-off distance should not be too small, otherwise there would not be any surrounding atom (situation sketched by the red (in the web version) circle in Fig. 2). Conversely, it should not be too large (sketched by the orange circle in Fig. 2) otherwise the local value of the transformation gradient would be unrealistically smoothed. Thus, as a rule of thumb, an appropriate cut-off distance should cover the nearest neighboring atoms and only them (situation sketched by the blue circle in Fig. 2). In the case of face-centered cubic (fcc), body-centered cubic (bcc) and hexagonal-close packed (hcp) lattices, the nearest neighbor distances are $\sqrt{2}a/2$, $\sqrt{3}a/2$ and a, respectively, where a is the lattice parameter. To avoid the singular behavior in Equation (4) if ΔX_i^{mn} becomes too small, an interior cut-off distance $r_{\mathrm{cutoff-in}} = 0.1a$ is used to filter out neighboring atoms that are too close. In the following, we use such three-dimensional finite difference methods (FDM) to calculate the components F_{ij}^{mn} of the transformation gradient, as well as all other derivatives.

Once local values at atomic positions are obtained, all the atoms are projected onto plane $(\vec{\mathbf{e}}_2, \vec{\mathbf{e}}_3)$, then two-dimensional linear interpolation is used to generate spatial field distributions in between atoms. The choice of a particular interpolation scheme does not interfere with the results qualitatively. The spatial field distributions and the contour lines are plotted by using the following steps: (1) All atoms are connected to create Delaunay triangles in the $(\vec{\mathbf{e}}_2, \vec{\mathbf{e}}_3)$ plane. When the triangles are constructed, it is ensured that no overlapping of triangles occurs. (2) Linear interpolation is used to search for all the intersection points of the triangle sides and contour lines. (3) The intersection points for each contour level are respectively connected with smoothed biharmonic–spline curves.

As an alternative, the least squares minimization method (LSMM) may also be used for the determination of the transformation gradient tensor **F**. For example, Gullett et al. (2008) recently computed the local transformation gradient tensor at atomic positions from the system. The transformation gradient links a vector in the reference configuration to a vector in the current configuration

$$\mathbf{\Delta x^{mn}} = \mathbf{F}\cdot\mathbf{\Delta X^{mn}} \tag{6}$$

where $\mathbf{F^m}$ is the value of the transformation gradient at atom m. Equation (6) can be applied for atom m and each of its neighbors to get a system of linear equations. However, these equations cannot be satisfied by a single mapping $\mathbf{F^m}$. To look for an optimal local transformation gradient $\widehat{\mathbf{F}}^{\mathbf{m}}$, the mapping errors are measured:

$$\boldsymbol{\phi}^{\mathbf{mn}} = \left(\mathbf{\Delta x^{mn}} - \widehat{\mathbf{F}}^{\mathbf{m}}\mathbf{\Delta X^{mn}}\right)^{\mathbf{T}}\left(\mathbf{\Delta x^{mn}} - \widehat{\mathbf{F}}^{\mathbf{m}}\mathbf{\Delta X^{mn}}\right) \tag{7}$$

and

$$\boldsymbol{\phi}^{\mathbf{m}} = \sum_{\mathbf{n}=1}^{\mathbf{N}}\left(\mathbf{\Delta x^{mn}} - \widehat{\mathbf{F}}^{\mathbf{m}}\mathbf{\Delta X^{mn}}\right)^{\mathbf{T}}\left(\mathbf{\Delta x^{mn}} - \widehat{\mathbf{F}}^{\mathbf{m}}\mathbf{\Delta X^{mn}}\right). \tag{8}$$

The optimal transformation gradient $\widehat{\mathbf{F}}^{\mathbf{m}}$ is obtained by minimizing $\boldsymbol{\phi}^{\mathbf{m}}$ with respect to the components of $\widehat{\mathbf{F}}$,

$$\partial\phi^m \Big/ \partial\widehat{F}_{ij} = \sum_n\Big(-2\Delta x_i^{mn}\Delta X_j^{mn} + 2\Delta x_j^{mn}\widehat{F}_{ik}\Delta X_k^{mn}\Big). \tag{9}$$

Setting Equation (9) equal to zero and the optimal transformation gradient is determined as

$$\mathbf{F} = \mathbf{AD}^{-1};\quad \mathbf{A} = \sum_{\mathbf{n}}\mathbf{\Delta x^{mn}\Delta X^{mnT}};\quad \mathbf{D} = \sum_{\mathbf{n}}\mathbf{\Delta X^{mn}\Delta X^{mnT}}. \tag{10}$$

The solution of Equation (10) requires the matrix inversion operation $\mathbf{D}^{-1}$, which may bring problems: (1) For some atoms, $\mathbf{D}$ is an ill-conditioned matrix, and its inversion may be wrongly calculated; (2) The inversion operation needs huge computing resource when the grain boundary consists of large numbers of atoms. Thus, the present methodology is more effective. We cross-checked our results on the copper tilt boundary presented in the following by also employing LSMM for a sake of comparison and validation. In both techniques, it is possible to use a cutoff radius larger than the closest neighbor distance and to consider nearest neighbor groups. In such instances, one weights the contribution of an atom n on the local value of $\mathbf{F}$ at atom m, depending on its group. For instance, Gullett et al. (2008) proposed a cubic spline weight function w_n:

$$w_n = \begin{cases} 1 - 6r_r^2 + 6r_r^3;\ r_r \le 0.5, \\ 2 - 6r_r + 6r_r^2 - 6r_r^3;\ 0.5 < r_r < 1, \\ 0;\ 1 \le r_r, \end{cases} \tag{11}$$

where the distance r_r for an atom n belonging to the ith nearest neighbor group is:

$$r_r = (r_{gi} - r_{g1}) \Big/ r_{cutoff}. \tag{12}$$

In the above, r_{g1} and r_{gi} are respectively the distances between the atom m and the closest neighbors in the first and ith neighbor groups. In the present work, we have checked that the first neighbor group ($r_{cutoff} = \sqrt{2}a/2$ in copper) yields satisfactory results and that using supplementary neighbor groups does not improve significantly the predictions. In that case, the weight function reduces to a step function:

$$w_n = \begin{cases} 1;\ r_{mn} \le r_{cutoff}, \\ 0;\ r_{mn} > r_{cutoff}. \end{cases} \tag{13}$$

3.2. Distortion, strain and rotation fields

In continuous media, the total displacement vector field $\mathbf{u} = \mathbf{x}-\mathbf{X}$ describes changes in the position of matter. This field is assumed to be single valued and continuous, possibly between atoms and below inter-atomic distances, so matter is assumed to be able to transmit stresses and couple stresses at this scale. The displacement gradient, also referred to as the distortion tensor, writes:

$$\mathbf{U} = \mathbf{grad\ u} = \mathbf{grad\ x} - \mathbf{I} = \mathbf{F} - \mathbf{I}, \tag{14}$$

where $\mathbf{I}$ is the second order identity tensor. The distortion is generally decomposed into strain and rotation. In a small perturbation approximation, the strain tensor $\boldsymbol{\varepsilon}$ is the symmetric part of the distortion:

$$\boldsymbol{\varepsilon} = \frac{1}{2}\left(\mathbf{U} + \mathbf{U}^{\mathbf{T}}\right). \tag{15}$$

In a finite deformation setting, the Green–Lagrange strain tensor is preferred:

$$\mathbf{E} = \frac{1}{2}\left(\mathbf{F}^{\mathbf{T}}\mathbf{F} - \mathbf{I}\right). \tag{16}$$

The rotation tensor $\boldsymbol{\omega}$ in a small displacement approximation is the skew-symmetric part of the distortion:

$$\boldsymbol{\omega} = \frac{1}{2}\left(\mathbf{U} - \mathbf{U}^{\mathbf{T}}\right). \tag{17}$$

and the associated rotation vector reads

$$\vec{\boldsymbol{\omega}} = -\frac{1}{2}\boldsymbol{\omega} : \mathrm{X} = \frac{1}{2}\mathbf{curl}\,\mathbf{u}, \tag{18}$$

where X is the alternating third order Levi-Civita tensor with components e_{ijk}, no possible confusion with the Lagrangian coordinate. In a finite deformation formulation, the rotation matrix $\mathbf{R}$ can be determined from the polar decomposition $\mathbf{F} = \mathbf{RW}$, by the following standard steps. First, the right Cauchy-Green tensor $\mathbf{C} = \mathbf{W}^{\mathbf{T}}\mathbf{W} = \mathbf{F}^{\mathbf{T}}\mathbf{F}$ is calculated and rotated into its principal orientation frame defined by the eigenvalues μ_i ($i = 1,2,3$). Then, projecting the square root of $\mathbf{C}$ onto the original frame yields $\mathbf{W}$ and the rotation tensor is finally obtained from $\mathbf{R} = \mathbf{FW}^{-1}$. The rotation vector $\vec{\boldsymbol{\omega}}$ associated with $\mathbf{R}$ is calculated as (Pantleon, 2008):

$$\omega_i = \frac{-e_{ijk}R_{jk}\beta}{2\sin\beta}; \quad \beta = \arccos((R_{kk} - 1)/2). \tag{19}$$

In the example of the copper tilt boundary presented below, the small perturbation and the finite deformation expressions are compared, particularly in terms of the resulting defect density fields.

4. Dislocation and generalized-disclination densities

The kinematic background describing lattice incompatibility due to the presence of dislocations and generalized-disclinations, seen as field densities (Acharya and Fressengeas, 2012), is recalled in this section. For mathematical notations and more details on the theory, the reader is referred to references (Acharya and Fressengeas, 2012; Berbenni et al., 2014). Dislocations introduce a discontinuity of the elastic displacement across some bounded surface in the body. As a result, the inverse elastic transformation tensor contains an incompatible, non-gradient part. Its curl yields Nye's dislocation density tensor (Nye, 1953; Kröner, 1980):

$$\boldsymbol{\alpha} = -\mathbf{curl}\left(\mathbf{F}^{-1}\right). \tag{20}$$

In a small strain formulation, the above equation writes:

$$\boldsymbol{\alpha} = \mathbf{curl}\,\mathbf{U}. \tag{21}$$

By decomposing the distortion into symmetric and skew-symmetric parts, one obtains:

$$\boldsymbol{\alpha} = \mathbf{curl}\,\boldsymbol{\varepsilon} - \boldsymbol{\kappa} + \mathbf{tr}(\boldsymbol{\kappa})\mathbf{I}. \tag{22}$$

In the above, $\boldsymbol{\kappa}$ is the second-order elastic curvature tensor. In a pure dislocation theory, the elastic rotation remains single-valued, and the curvature is the gradient of the rotation vector:

$$\boldsymbol{\kappa} = \mathbf{grad}(\vec{\boldsymbol{\omega}}). \tag{23}$$

If standard disclinations are present in the body (deWit, 1970; Fressengeas et al., 2011), the elastic rotation encounters discontinuities. Hence, the curvature tensor contains an incompatible part whose curl yields deWit's disclination density tensor:

$$\boldsymbol{\theta} = \mathbf{curl}\,\boldsymbol{\kappa}. \tag{24}$$

Because the elastic rotation is multi-valued in the presence of disclinations, the elastic distortion is undefined. Hence, in a small strain setting, Equation (22) is to be used instead of Equation (21). In a reference Cartesian frame $(\vec{\mathbf{e}}_1, \vec{\mathbf{e}}_2, \vec{\mathbf{e}}_3)$, the

continuous components α_{ij} (respectively θ_{ij}) of the tensor $\boldsymbol{\alpha}$ (respectively $\boldsymbol{\theta}$) express a discontinuity of the elastic displacement u_i (respectively ω_i) per unit surface introduced by a dislocation (respectively disclination) line having line direction along $\vec{\mathbf{e}}_\mathbf{j}$. Hence, the tensors $\boldsymbol{\alpha}$ and $\boldsymbol{\theta}$ are continuous renditions of the discontinuities of the elastic displacement and rotation introduced by dislocations and disclinations. The associated point–wise measures of incompatibility are the Burgers and Frank vectors, defined as:

$$\vec{\mathbf{b}} = \int_S \left(\boldsymbol{\alpha} - \left(\boldsymbol{\theta}^\mathbf{T} \times \mathbf{r}\right)^\mathbf{T}\right) \cdot \mathbf{n}\, dS, \tag{25}$$

$$\vec{\boldsymbol{\Omega}} = \int_S \boldsymbol{\theta} \cdot \mathbf{n}\, dS. \tag{26}$$

In Equation (25), $\mathbf{r}$ is a position vector. The above two equations are scale-dependent measures of lattice incompatibility. By choosing an appropriate surface S, one can measure the Burgers and Frank vectors of isolated defects as well as those of an ensemble of defects. In the example of the tilt boundary presented below, these equations will be used to quantify both the nanoscale incompatibility of the individual defects composing the grain boundary and the mesoscale overall incompatibility of the boundary.

Similarly, generalized-disclination densities were recently introduced in order to render in a continuous fashion the discontinuities of the elastic distortion tensor across bounded surfaces in a body (Acharya and Fressengeas, 2012). If the elastic distortion remains single-valued in a body, the third-order elastic second-distortion tensor $\mathbf{G}$ is defined, in a "small strain" formulation, as the gradient of the distortion:

$$\mathbf{G} = \mathbf{grad}\, \mathbf{U}. \tag{27}$$

However, if discontinuities of the elastic distortion are present, the tensor $\mathbf{G}$ contains an additional incompatible part whose curl yields the third-order generalized-disclination density tensor:

$$\boldsymbol{\pi} = \mathbf{curl}\, \mathbf{G}. \tag{28}$$

In a reference Cartesian frame $(\vec{\mathbf{e}}_1, \vec{\mathbf{e}}_2, \vec{\mathbf{e}}_3)$, the components π_{ijk} of the tensor $\boldsymbol{\pi}$ express a discontinuity of the distortion U_{ij} per unit surface introduced by a generalized-disclination line having line direction along $\vec{\mathbf{e}}_\mathbf{k}$. In the manner of tensors $\boldsymbol{\alpha}$ and $\boldsymbol{\theta}$, $\boldsymbol{\pi}$ is an areal continuous rendition of the discontinuity of the elastic distortion in a body. The associated point–wise measure of incompatibility is the jump of distortion $\boldsymbol{\Pi}$:

$$\boldsymbol{\Pi} = \int_S \boldsymbol{\pi} \cdot \mathbf{n}\, dS. \tag{29}$$

Like Equations (25) and (26), Equation (29) is a scale-dependent measure of the incompatibility introduced by generalized-disclinations. The generalized-disclination density tensor $\boldsymbol{\Pi}$ complements the standard disclination density $\boldsymbol{\theta}$ by adding a discontinuity of strain to that of the rotation, such that the total distortion is discontinuous. The following relation links both tensors:

$$\boldsymbol{\pi} = \boldsymbol{\xi} - \mathrm{X} \cdot \boldsymbol{\theta}, \tag{30}$$

where the third-order tensor $\boldsymbol{\xi}$ is associated with discontinuities of the elastic strain tensor. In the presence of generalized-disclinations, the definition of the dislocation density tensor becomes (Acharya and Fressengeas, 2012)

$$\boldsymbol{\alpha} = -\mathbf{G} : \mathrm{X}, \tag{31}$$

because discontinuities in the distortion $\mathbf{U}$ preclude calculating unequivocally its curl, whereas $\mathbf{G}$ remains unambiguously defined. This equation is used to calculate the dislocation density at small strains and the associated Burgers vector follows from Equation (25). From displacement and distortion fields defined at a very small resolution length-scale, we expect detailed maps of the strain, rotation, curvature and second-distortion, as well as a detailed account of the dislocation and generalized-disclination fields in the GB area.

5. Application to the Σ37 (610)[100] symmetric tilt boundary

5.1. Strain, curvature, disclination and dislocation density fields

The methods described above are now applied to the 18.9° symmetric tilt boundary atomic built is Section 2. As aforementioned, the reference configuration is the low-energy relaxed structure (colored atoms in Fig. 1) and the initial

configuration is the un-relaxed configuration (black and white atoms in Fig. 1). As can be seen in Fig. 1, large deformations occur during the relaxation process. They appear to be located in small nanometer thick areas close to the structural units, whereas they are relatively small far away from the boundary. For example, the segment AC between atoms A and C, rotates by a large clockwise angle, from 36° with respect to the boundary plane in the reference configuration, down to 9.5° in the current deformation. Due to symmetry with respect to the boundary, the segment AB encounters the opposite anti-clockwise rotation. While the incompatible strain and second-distortion fields derive from the presence of defects, additional compatible (gradient) elastic strain and second-distortion fields allow satisfying the balance of equilibrium and boundary conditions in the body (Acharya, 2001; Berbenni et al., 2014). Because balance of equilibrium and (periodic) boundary conditions are satisfied along the simulated atomistic relaxation process, the compatible elastic strain and second-distortion fields are included in the fields obtained from the simulation. However, the curl operation used in Equations (16), (18), (20) and (24) to define the dislocation, disclination and generalized-disclination densities extracts only the incompatible parts and leaves aside the compatible parts. The reference Cartesian frame used for the derivation of elastic and defect density fields is shown in Fig. 1. Although the framework is completely three-dimensional, the following figures are restricted to the plane $(\vec{\mathbf{e}}_2, \vec{\mathbf{e}}_3)$, which is sufficient for the description of a symmetrical tilt boundary (Fressengeas et al., 2014). The mathematical notations for calculations of second-order and third-order curls and permutations are provided in the Appendix.

The in-plane Green–Lagrange strains are shown in Fig. 3. The maximum values of the extensions/contractions E_{22} and E_{33} are essentially located at the extremities of the structural units, while the shear strain E_{23} is found all along the boundary with

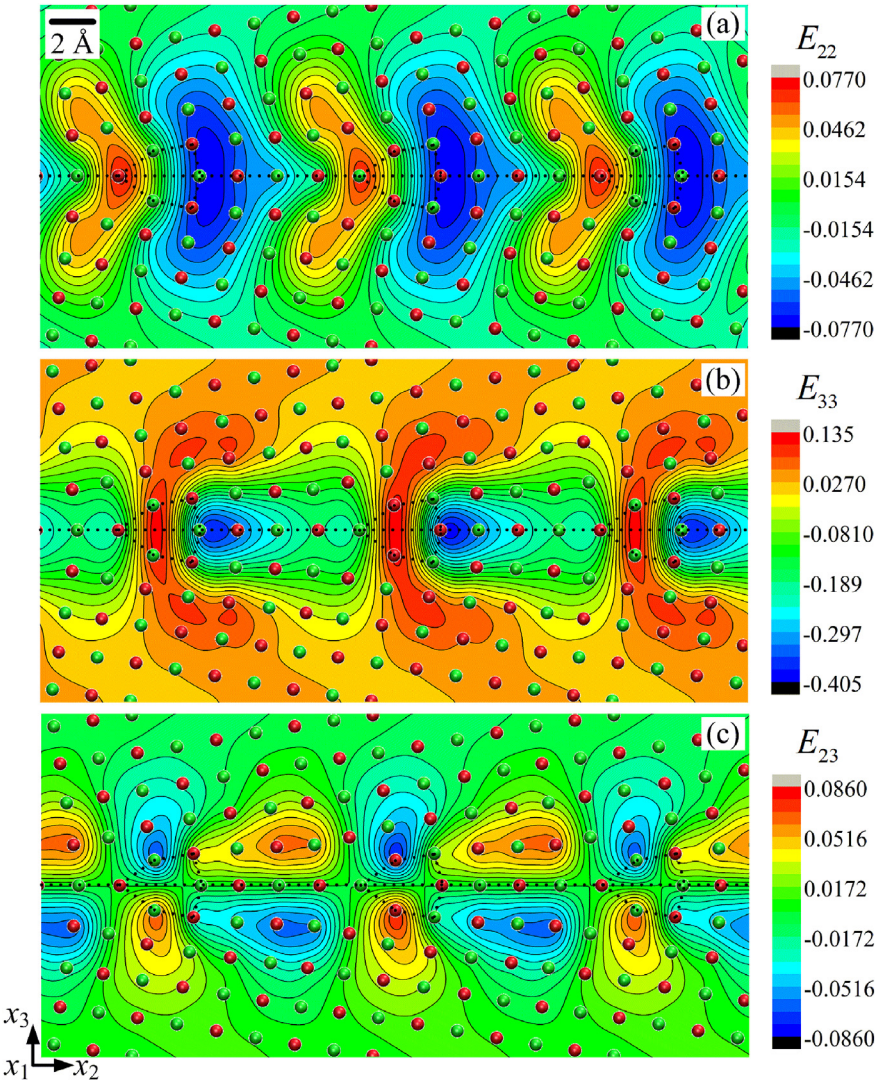

Fig. 3. Close-up showing the in-plane Green–Lagrange tensile strains (a) E_{22}, (b) E_{33} and shear strain (c) E_{23} on top of the relaxed atomic structure of the simulated Σ37 (610)[100] copper tilt boundary of misorientation 18.9°. (For interpretation of the references to color in this figure legend, the reader is referred to the web version of this article.)

alternate signs across the boundary plane. Note the magnitudes of the strains that can reach values as high as 40% at some places, so it is more appropriate to use the finite deformation setting rather than the small-strain setting for computing the strain and the strain-related tensors. Similarity of these fields, in particular the shear strain, with those recently predicted by using disclination fields for the same boundary is striking (Fressengeas et al., 2014).

The tilt rotation ω_1 calculated in the finite strain formulation is shown in Fig. 4. Like the strains, it is essentially located within a nanometer thick layer along the boundary. The two strong and localized spots of opposite magnitude across the grain boundary at each structural unit are in agreement with the rotation of segments AC and AB discussed above, and clearly show that the structural units accommodate most of the change of misorientation across the grain boundary. The maximum local magnitude of the tilt rotation is found to be the order of 5° (*i.e.*, 0.07 rad).

The curvature components κ_{12} and κ_{13} are shown in Fig. 5. The curvature κ_{12} reflects the variations of the tilt rotation ω_1 along the boundary and is globally balanced (the average value in the figure is zero), while the strong negative curvature κ_{13} located inside the structural units is unbalanced and stems from the fast change of sign of the rotation ω_1 across the units. These fields are consistent with the tilt character of the boundary and their similarity with those recently predicted by using disclination fields for the same boundary is again striking (Fressengeas et al., 2014).

The resulting wedge disclination density field θ_{11} in the tilt boundary area is shown in Fig. 6, still using the finite rotation formulation. We recall that such a density reflects disclinations lines along the axis x_1 and rotation discontinuities around the same axis. Disclination dipoles are found at the ends of the structural units, in excellent agreement with the construction previously proposed for the same boundary (Fressengeas et al., 2014). In the continuous modeling (Fressengeas et al., 2014), the curvature tensor component κ_{13} ranges from -0.45–1.48 rad/Å, the disclination density tensor component θ_{11} ranges from -3 to 3 rad/Å^2, 1–2 orders of magnitude larger the results in the present work. There is no contradiction however, because their distribution of disclination dipoles is much more localized in small areas in the structural units than in the present work. The comparison of Figs. 3 and 6 shows that the lattice opens at a positive disclination pole and closes at a negative one. The comparison of Figs. 4 and 6 further reveals that the fast change of sign of the tilt rotation across the structural units is delimited by the wedge disclination dipoles. Hence, the structural units delimit a bounded surface of rotation discontinuity (or of strong gradient value in a regularized framework) in the crystal along the boundary plane.

The Frank vector quantifying this discontinuity is measured by using Equation (26). The surface patch S that is used is delimited by the blue dotted lines in Fig. 6. It contains a wedge disclination dipole. Because the polarity of the disclinations offsets within such a surface, the integral (26) is zero. By using the absolute values of the disclination density, this integral is non-zero and equals twice the Frank vector magnitude of the disclination single poles. The value of the Frank vector magnitude is found to be approximately $\Omega_1 = 10°$ and corresponds effectively to a discontinuity of the tilt rotation. Convergence of this value with the height of the surface S in the direction normal to the boundary plane was checked and is shown in Fig. 7. We have chosen the wedge disclination density field to compare our approach with the least squares minimization method (LSMM) (Gullett et al., 2008; Zimmerman et al., 2009) and simultaneously check the effect of using a small strain setting rather than a finite strain formulation. As shown in Fig. 8, the disclination density field obtained within a small perturbation framework is very similar to that shown in Fig. 6, and a very good agreement between the FDM and LSMM calculation methods is observed, suggesting accuracy of our approach. According to Equations (23) and (24), the disclination density tensor $\boldsymbol{\theta}$ is estimated from the second spatial derivatives of the rotation vector $\underset{\sim}{\boldsymbol{\omega}}$ but not on the strain tensor. As seen in Fig. 4, the maximum local magnitude of the tilt rotation is as small as 0.07 rad, so the disclination density field obtained within a small perturbation framework (Fig. 8b) is very similar to that calculated from finite rotation formulation (Fig. 6).

The dislocation density fields obtained from Equation (20) are shown in Fig. 9. Edge dislocation densities α_{21} and α_{31} are obtained. The component α_{21} renders dislocation lines along the axis x_1 and Burgers vector along the axis x_2, while the component α_{31} renders dislocation lines along the axis x_1 and Burgers vector along the axis x_3. Hence, consistent with the tilt character of the boundary, one obtains a full description of the Burgers vector in the plane of the figure, for edge dislocations having line direction along the tilt axis. The distribution of dislocation density α_{21} is balanced and is essentially found in the

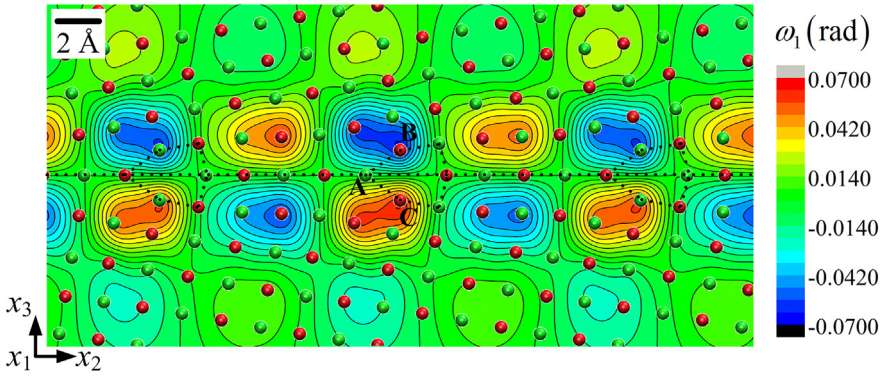

Fig. 4. Close-up showing the tilt rotation ω_1 on top of the relaxed atomic structure of the simulated Σ37 (610)[100] copper tilt boundary of misorientation 18.9°.

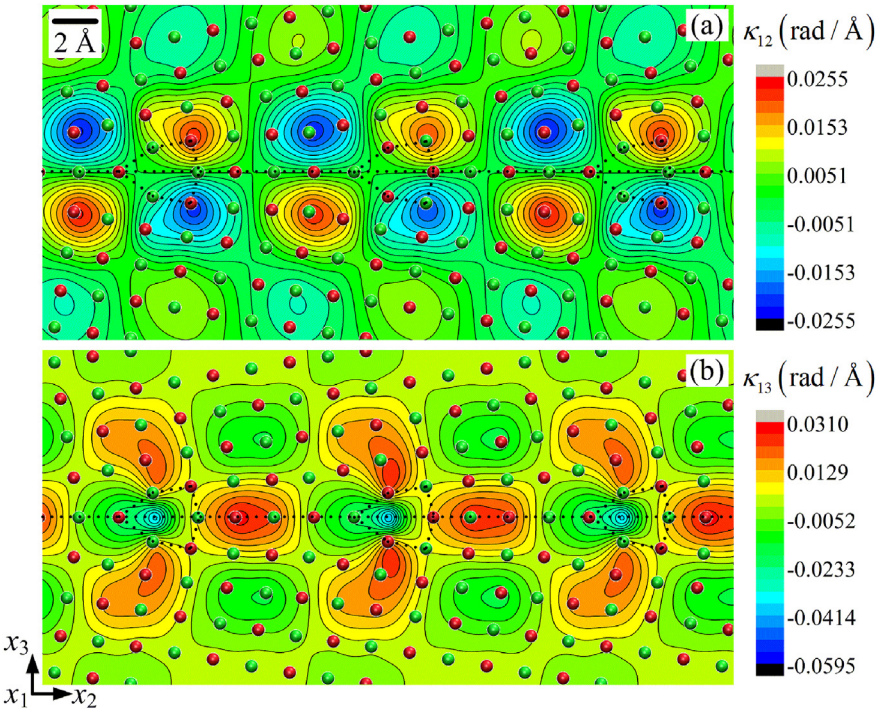

Fig. 5. Close-up showing curvatures (a) κ_{12} and (b) κ_{13} on top of the relaxed atomic structure of the simulated Σ37 (610)[100] copper tilt boundary of misorientation 18.9°.

form of dipoles across the structural units. However, the distribution of dislocation density α_{31} is unbalanced. According to Equation (21), the net Burgers vector can be calculated from the distribution of dislocation and disclination densities over a surface S in the plane. Similarly to the Frank vector, the Burgers vector has a dependence on the selection of the circuit C. As shown in Fig. 6, the length of the integration box in the x_2 direction corresponds to a periodic sequence of atoms along the boundary plane, but its height in the x_3 direction may be varied. In Fig. 7, the components b_2 and b_3 of the Burgers vector are plotted as functions of the integration box height. For this grain boundary, these components are respectively the resulting Burgers vectors parallel and normal to the boundary plane, of partial edge dislocations with line parallel to the GB tilt axis, for each atomic structural unit. The overall Burgers vector parallel to the boundary b_2 is zero, consistent with the balanced distribution of the associated dislocation density α_{21}. However, as shown in Fig. 7, the overall Burgers vector perpendicular to the boundary plane b_3 is approximately −0.24 nm per structural unit. These features are again consistent with the tilt character of the boundary. Note further that overlapping of both dislocation density fields suggest the decomposition of the Burgers vector perpendicular to the boundary plane into two partial edge dislocations in each grain in the middle of the

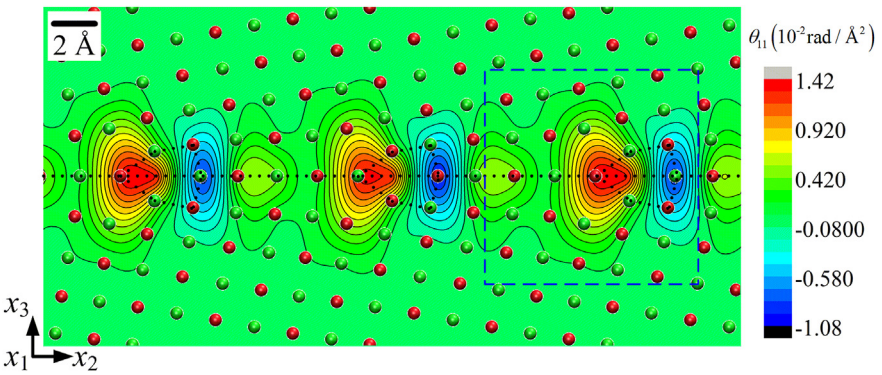

Fig. 6. Close-up showing the wedge disclination density field θ_{11} on top of the relaxed atomic structure of the simulated Σ37 (610)[100] copper tilt boundary of misorientation 18.9°. The blue dotted lines delimit the surface S used for the calculation of the Frank and Burgers vectors associated with structural units. (For interpretation of the references to color in this figure legend, the reader is referred to the web version of this article.)

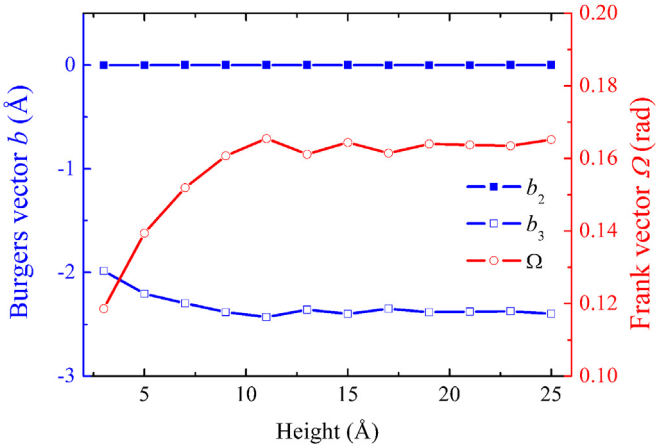

Fig. 7. Values of Frank/Burgers vectors as a function of the height of the surface S shown in Fig. 6.

structural units. Because we have access to the net Burgers vector of the structural units and their spacing, it is tempting to compare with the Frank dislocation model of grain boundaries (Frank, 1950). For a tilt boundary, Frank's relation writes $b/h = 2\sin(\theta/2)$, where b is the Burgers vector magnitude of edge dislocations, h is their spacing and θ is the misorientation. Using the present values, $h = 1.115$ nm and $b = 0.24$ nm, the predicted misorientation value is $\theta = 12.36°$, lower than the actual value $\theta = 18.9°$. This discrepancy suggests that tilt boundaries cannot be consistently described by pure edge dislocation arrays at large misorientations.

The present dislocation/disclination distribution is more complex than the dipolar disclination structure proposed in recent modeling of the same boundary (Fressengeas et al., 2014). In particular, no dislocation density was used in this paper in producing the tilt angle. The distribution of the elastic energy density fields and the excess energies obtained from these alternative representations will be compared in a forthcoming publication.

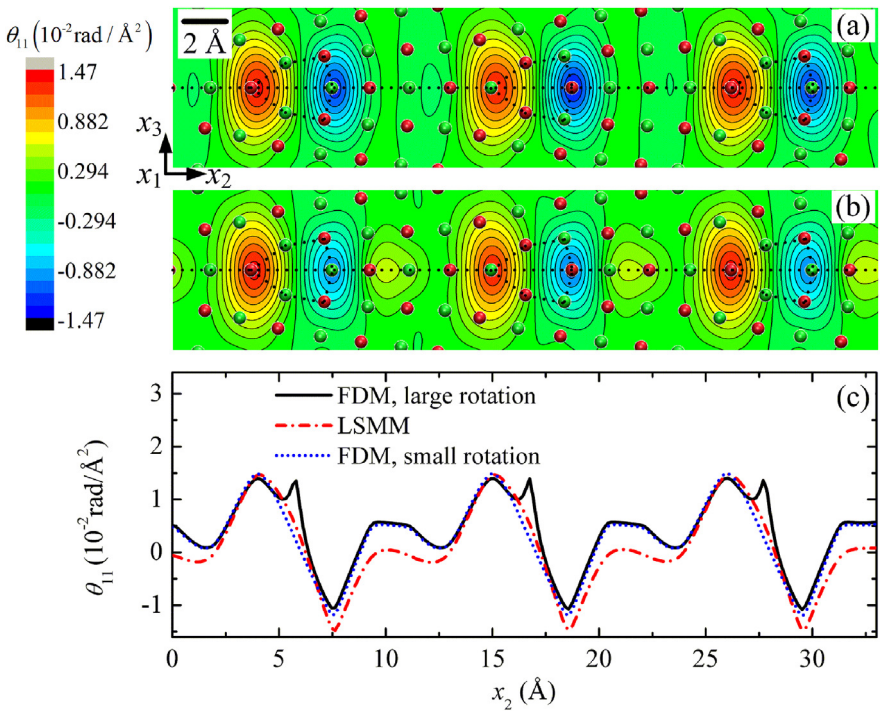

Fig. 8. Wedge disclination density field θ_{11} calculated by (a) least squares minimization method (LSMM) (b) the present finite difference method (FDM), within a small rotation setting. (c) Profiles of the disclination density along the boundary plane are compared with the finite strain solution shown in Fig. 6.

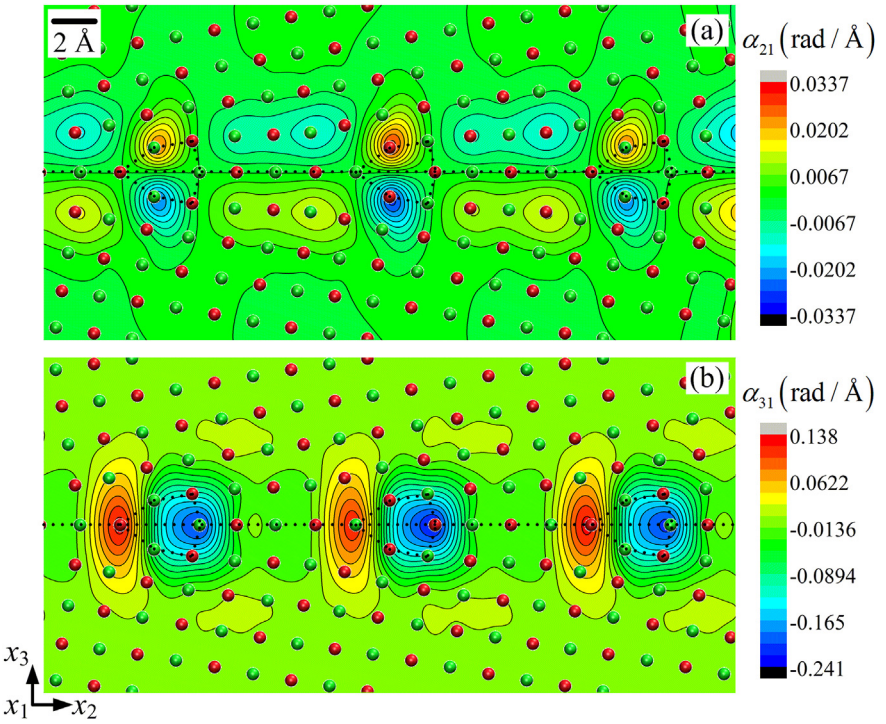

Fig. 9. Close-up showing edge dislocation density components (a) α_{21} and (b) α_{31} on top of the relaxed atomic structure of the simulated Σ37 (610)[100] copper tilt boundary of misorientation 18.9°.

5.2. Generalized-disclination density fields

The tilt boundary essentially produces a discontinuity in the lattice rotation ω_1. However, local shear strain discontinuities can be observed in Fig. 3c, which we now investigate in relation with the generalized-disclination fields. From Equation (28), by restricting ourselves to discontinuities of the in-plane distortions U_{22}, U_{33}, U_{23} and U_{32}, the components π_{221}, π_{331}, π_{231} and π_{321} are involved. These four components have a common defect line direction along the axis x_1, parallel to the tilt axis. From Equation (30), the components π_{321}, π_{231}, $\xi_{321} = \xi_{231}$ and the standard wedge disclination density θ_{11} satisfy:

$$\pi_{321} = \xi_{321} + \theta_{11}, \tag{32}$$

$$\pi_{231} = \xi_{231} - \theta_{11}, \tag{33}$$

The component π_{321} characterizes the discontinuity of the distortion U_{32}. Its field is shown in Fig. 10, together with the density field $\xi_{321} = \xi_{231}$ characterizing the discontinuity of the elastic strain $\varepsilon_{23} = \varepsilon_{32}$. Strikingly, the ξ_{321} density field has the same dipolar structure as the standard wedge disclination density field θ_{11}. Dipoles with similar polarity and magnitude are indeed observed at the ends of the structural units. Thus, in addition to the discontinuity of tilt rotation, the structural units induce a discontinuity of the shear strain ε_{23}. Such a result is reminiscent of recent experimental observations of elastic strain fields around structural units in a symmetrical tilt boundary in Si, where the shear strain exhibits sign changes across the boundary (Couillard et al., 2013). From Equation (32), the contributions of ξ_{321} and θ_{11} add, such that the component π_{321} is relatively more important than the component π_{231}. Therefore, the structural units induce a significant discontinuity of the distortion U_{32}. By using Equation (29) and the same surface S, the magnitude of this distortion discontinuity, *i.e.*, the strength of the generalized-disclination π_{321} dipole, is found to be approximately 0.31 (31%). It includes both a shear discontinuity and a rotation discontinuity. In contrast, from Equation (29), the contributions ξ_{321} to shear discontinuity and θ_{11} to rotation discontinuity cancel, such that the component π_{231} is relatively small. The discontinuity of the distortion U_{23} is found to be 0.05 (5%), 6 times smaller than the discontinuity of the distortion U_{32}. The observed rotation discontinuity does receive an interpretation within the framework of the standard disclination theory, but the strain discontinuity does not. Neither of them receives a consistent interpretation in a pure dislocation-based theory.

We now focus on discontinuities of the stretches U_{22}, U_{33}, or (ε_{22},ε_{33}). The associated generalized disclination densities π_{221} and π_{331} are shown in Fig. 11. For both components, narrow vertical dipoles are found across the structural units. These dipoles are clearly associated with the swift sign change of the stretch occurring within the structural units along the boundary. Their strength is measured to be 0.083 for a single π_{221} pole and 0.173 for a single π_{331} pole. These values

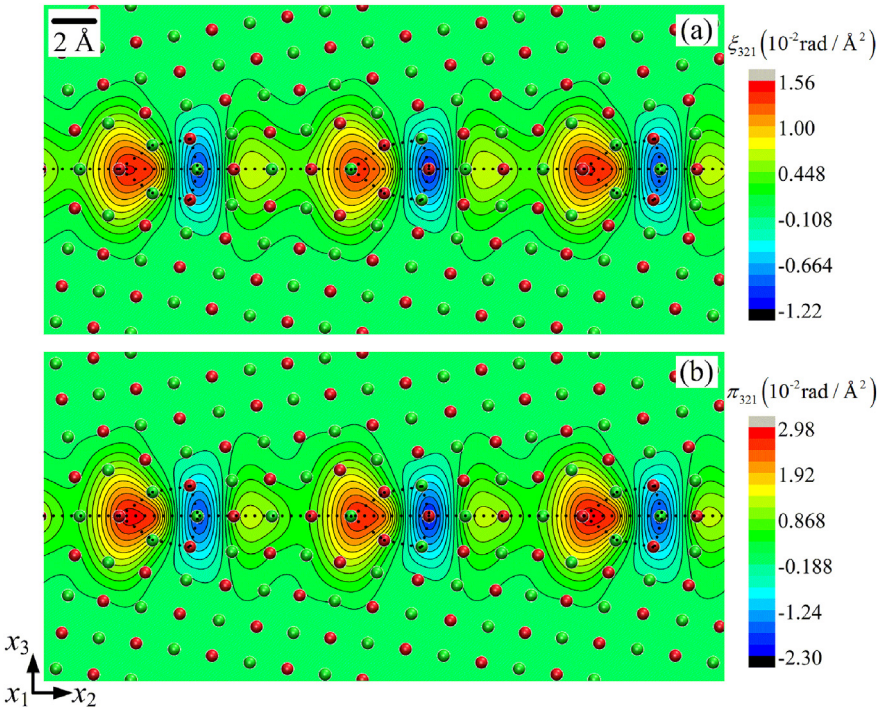

Fig. 10. Close-up showing the generalized-disclination component π_{321} on top of the relaxed atomic structure of the simulated Σ37 (610)[100] copper tilt boundary of misorientation 18.9°. In (a), only the elastic strain is used to calculate the component ξ_{321}. In (b), the elastic distortion is used to calculate the component π_{321}.

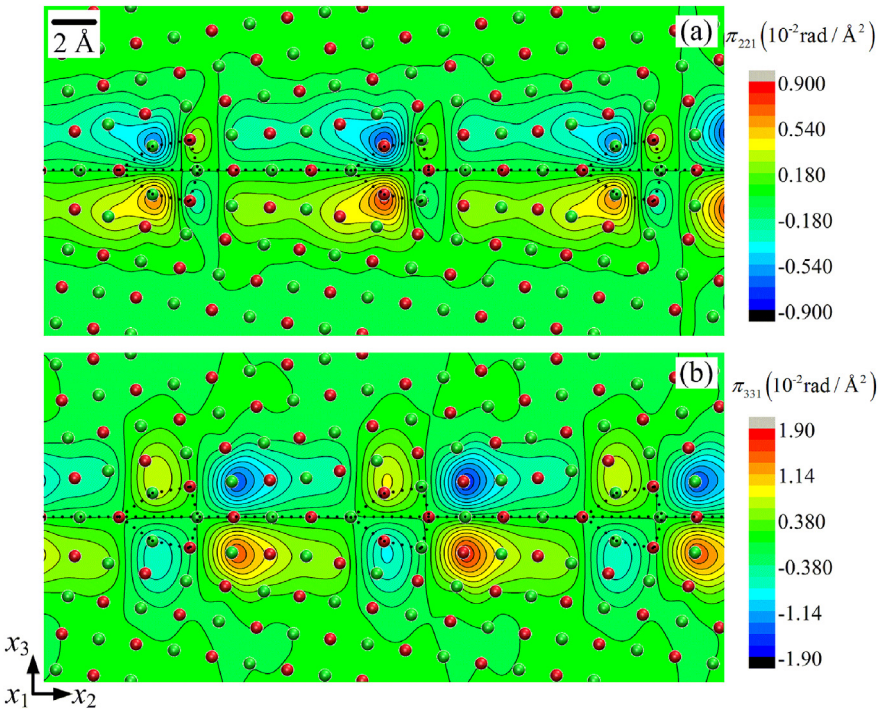

Fig. 11. Close-up showing the generalized-disclination components (a) π_{221} and (b) π_{331} on top of the relaxed atomic structure of the simulated Σ37 (610)[100] copper tilt boundary of misorientation 18.9°.

characterize the discontinuity of stretch delimited by the dipoles. Using a surface patch S containing a period of atomic scale defects along the interface, and extending far away on both sides of the interface (say at least 2.5 nm), it is nevertheless found from Equation (29) that the integrals $\int_{221} \mathrm{d}S$, $\int_{331} \mathrm{d}S$ are zero, due to symmetry of the generalized-disclination fields.

Therefore the stretch incompatibility manifested locally in the boundary area is no more observed at mesoscale when the viewpoint is more distant. Clearly, the stretch discontinuity cannot receive a consistent interpretation within the framework of pure dislocation-based theories, or even within dislocation/standard disclination theories, because the strain field retains continuity in both theories. We note further that, since the stretch incompatibility is no more manifested at mesoscale, the elastic energy density of the boundary arising from stretch at inter-atomic scale is irreparably lost in a coarse-graining procedure.

6. Conclusions

The present paper proposes a general "bottom-up" procedure that allows modeling the atomic structure of GBs by appropriate fields of dislocation and generalized-disclination densities smoothly defined at inter-atomic scale. The "bottom-up" adjective refers to the construction of displacement fields characterizing the crystal lattice at the inter-atomic resolution length scale, on the basis of the discrete atomic positions in the GB area. From the differences in the atomistic configuration between the initial un-relaxed and relaxed configurations, a numerical method is developed to calculate the transformation gradient. The latter allows deriving kinematic and dislocation/generalized-disclination fields that are continuous at inter-atomic scale and characterize the relaxed atomistic configuration. Applied to a simple symmetrical tilt boundary in copper, the analysis reveals previously unseen complexity of its structure. Indeed, unexpected features are evidenced, such as the presence of localized shear and stretch distortion discontinuities and second-order incompatibility associated with the presence of generalized-disclination dipoles in the structural units. In addition, the analysis confirms the presence of standard wedge disclination dipoles similar those proposed in previous work by the authors. Applied here to reconstruct and interpret a symmetrical tilt boundary built from molecular dynamics calculations, the analysis reveals previously unseen complexity of this self-organized structure. Indeed, unexpected features are evidenced, such as the presence of localized shear and stretch distortion discontinuities in the structural units and second-order shear incompatibility associated with the presence of generalized-disclination dipoles. In addition, the analysis confirms the presence of standard wedge disclination dipoles similar those evidenced in previous work by the authors. The present method can be employed to investigate more general interfaces, such as hetero-interfaces and interphases. It is available to analyze experimental images from high-resolution microscopy as well. Future work includes the application of the technique to the complex GB structures in olivine (Cordier et al., 2014).

The benefits of such a discrete-to-continuum crossover are two-fold. First, smoothness of the description at inter-atomic length scale is useful because it allows coping with core properties of the GBs. Indeed, when viewed at a sufficiently small scale, the lattice defects and their associated distributions of elastic fields are better described by suitably localized smooth density fields than by singularities. Second, the continuity of the description of grain boundaries at nanoscale provides a natural background for coarse-grained theories of crystal defect ensembles at mesoscale or higher, which necessarily have continuous character (Taupin et al., 2015). Indeed, coarse-graining such nanoscale investigations within a continuous framework, by keeping track as much as possible of the incompatibility of the elastic distortion and second distortion observed at inter-atomic scale, opens opportunities for simulating the influence of GB structure on the mechanical response of polycrystalline aggregates.

Acknowledgments

This work was supported by funding from the European Research Council under the ERC Grant No. 290424 – RheoMan.

Appendix

A bold symbol denotes a tensor. When there may be ambiguity, an arrow is superposed to represent a vector: $\vec{\mathbf{V}}$. The tensor $\mathbf{A}\cdot\mathbf{B}$, with rectangular Cartesian components $A_{ik}B_{kj}$, represents multiplication of the tensors $\mathbf{A}$ and $\mathbf{B}$. The symbol $\mathbf{A}$: denotes the trace inner product of the two second order tensor $\mathbf{A}:\mathbf{B} = A_{ij}B_{ij}$, in rectangular Cartesian components, or the product of a higher order tensor with a second order tensor, *e.g.*, $\mathbf{A}:\mathbf{B} = A_{ijkl}B_{kl}$. The **grad** and **curl** operations for different order tensors are defined row by row, in analogy with the vectorial case. In rectangular Cartesian components:

$$(\mathbf{grad}\,\mathbf{V})_{ij} = \mathbf{V}_{i,j} \tag{A.1}$$

$$(\mathbf{grad}\,\mathbf{A})_{ijk} = \mathbf{A}_{ij,k} \tag{A.2}$$

$$(\mathbf{curl}\,\mathbf{A})_{ij} = e_{jkl}\mathbf{A}_{il,k} = -(\mathbf{grad}\,\mathbf{A} : \mathrm{X})_{ij} \tag{A.3}$$

$$(\mathbf{curl}\,\mathbf{A})_{ijk} = e_{klm}\mathbf{A}_{ijm,l} \tag{A.4}$$

where e_{jkl} is a component of the third-order alternating Levi-Civita tensor X and the spatial derivative with respect to a Cartesian coordinate is indicated by a comma followed by the component index. A rotated vector $\overrightarrow{\mathbf{A}}$ is associated with the second order tensor $\mathbf{A}$ by using its trace inner product with tensor X:

$$\left(\overrightarrow{\mathbf{A}}\right)_k = -\frac{1}{2}(\mathbf{A} : \mathrm{X})_k = -\frac{1}{2}e_{ijk}A_{ij}. \tag{A.5}$$

In the component representation, the spatial derivative with respect to a Cartesian coordinate is indicated by a comma followed by the component index.

References

Acharya, A., 2001. A model of crystal plasticity based on the theory of continuously distributed dislocations. J. Mech. Phys. Solids 49, 761.
Acharya, A., Fressengeas, C., 2012. Coupled phase transformations and plasticity as a field theory of deformation incompatibility. Int. J. Frac. 174, 87–94.
Berbenni, S., Paliwal, B., Cherkaoui, M., 2013. A micromechanics-based model for shear-coupled grain boundary migration in bicrystals. Int. J. Plast. 44, 68–94.
Berbenni, S., Taupin, V., Fressengeas, C., Djaka, K.S., 2014. A numerical spectral approach for solving elasto-static field dislocation and g-disclination mechanics. Int. J. Solids Struct. 51, 4157–4175.
Bozhko, S.I., Taupin, V., Lebyodkin, M., Fressengeas, C., Levchenko, E.A., Radikan, K., Lübben, O., Semenov, V.N., Shvets, I.V., 2014. Disclinations in C_{60} molecular layers on WO_2/W(110) surfaces. Phys. Rev. B 90, 214106.
Cordier, P., Demouchy, S., Beausir, B., Taupin, V., Barou, F., Fressengeas, C., 2014. Disclinations provide the missing mechanism for deforming olivine-rich rocks in the mantle. Nature 507, 51–56.
Couillard, M., Radtke, G., Botton, G.A., 2013. Strain fields around dislocation arrays in a Σ9 silicon bicrystal measured by scanning transmission electron microscopy. Phil. Mag. 93, 1250–1267.
deWit, R., 1970. Linear theory of static disclinations. In: Simmons, J.A., deWit, R., Bullough, R. (Eds.), Fundamental Aspects of Dislocation Theory, Spec. Publ. 317, vol. I. Nat. Bur. Stand., US, pp. 651–673.
Frank, F.C., 1950. The resultant content of dislocations in an arbitrary intercrystalline boundary. In: Symposium on the Plastic Deformation of Crystalline Solids, Office of Naval Research Pittsburgh, Pennsylvania, p. 150.
Fressengeas, C., Taupin, V., Capolungo, L., 2011. An elasto-plastic theory of dislocation and disclination fields. Int. J. Solids Struct. 48, 3499–3509.
Fressengeas, C., Taupin, V., Capolungo, L., 2014. Continuous modeling of the structure of symmetric tilt boundaries. Int. J. Solids Struct. 51, 1434–1441.
Gullett, P.M., Horstemeyer, M.F., Baskes, M.I., Fang, H., 2008. A deformation gradient tensor and strain tensors for atomistic simulations. Model. Simul. Mater. Sci. Eng. 16, 015001.
Hirel, P., 2015. Atomsk: a tool for manipulating and converting atomic data files. Comput. Phys. Comm. http://dx.doi.org/10.1016/j.cpc.2015.07.012.
Hÿtch, M.J., Snoeck, E., Kilaas, R., 1998. Quantitative measurement of displacement and strain fields from HREM micrographs. Ultramicroscopy 74, 131–146.
Hÿtch, M.J., Putaux, J.L., Penisson, J.M., 2003. Measurement of the displacement by field of dislocations to 0.03 A electron microscopy. Nature 423, 270–273.
Hÿtch, M.J., Putaux, J.L., Thibault, J., 2006. Stress and strain around grain-boundary dislocations measured by high-resolution electron microscopy. Philos. Mag. 86, 4641–4656.
Kröner, E., 1980. Continuum theory of defects. In: Balian, R., et al. (Eds.), Physics of Defects, pp. 218–314. North Holland, Amsterdam.
Martyna, G.J., Tobias, D.J., Klein, M.L., 1994. Constant pressure molecular dynamics algorithms. J. Chem. Phys. 101, 4177–4189.
Mishin, Y., Mehl, M.J.D.A., Papaconstantopoulos, A.F.V., Kress, J.D., 2001. Structural stability and lattice defects in copper: Ab initio, tight-binding, and embedded-atom calculations. Phys. Rev. B 63, 224106.
Nye, J.F., 1953. Some geometrical relations in dislocated crystals. Acta Metall. 1, 153.
Pantleon, W., 2008. Resolving the geometrically necessary dislocation content by conventional electron backscattering diffraction. Scr. Mater. 58, 994–997.
Plimpton, S., 1995. Fast parallel algorithms for short-range molecular dynamics. J. Comput. Phys. 117, 1.
Prieto-Depedro, M., Martin-Bragado, I., Segurado, J., 2015. An atomistically informed kinetic Monte Carlo model of grain boundary motion coupled to shear deformation. Int. J. Plast. 68, 98–110.
Rösner, H., Kübel, C., Ivanisenko, Y., Kurmanaeva, L., Divinski, S.V., Peterlechner, M., Wilde, G., 2011. Strain mapping of a triple junction in nanocrystalline Pd. Acta Mater 59, 7380–7387.
Rouvière, J.L., Sarigiannidou, E., 2005. Theoretical discussions on the geometrical phase analysis. Ultramicroscopy 106, 1–17.
Sutton, A.P., Vitek, V., 1983. On the structure of tilt grain boundaries in cubic metals. I. Symmetrical tilt boundaries. Philos. Trans. R. Soc. Lond. A 309, 1.
Taupin, V., Capolungo, L., Fressengeas, C., 2014. Disclination mediated plasticity in shear-coupled boundary migration. Int. J. Plast. 53, 179–192.
Taupin, V., Capolungo, L., Fressengeas, C., Upadhyay, M., Beausir, B., 2015. A mesoscopic theory of dislocation and disclination fields for grain boundary-mediated crystal plasticity. Int. J. Solids Struct. 71, 277–290.
Tschopp, M.A., Spearot, D.E., McDowell, D.L., 2008. Influence of grain boundary structure on dislocation nucleation in FCC metals. In: Hirth, J.P. (Ed.), Dislocations in Solids, vol. 14. Elsevier Amsterdam, p. 43.
Tucker, G.J., Foiles, S.M., 2015. Quantifying the influence of twin boundaries on the deformation of nanocrystalline copper using atomistic simulations. Int. J. Plast. 65, 191–205.
Tucker, G.J., Zimmerman, J.A., McDowell, D.L., 2010. Shear deformation kinematics of bicrystalline grain boundaries in atomistic simulations. Model. Simul. Mater. Sci. Eng. 18, 015002.
Tucker, G.J., Tiwari, S., Zimmerman, J.A., McDowell, D.L., 2012. Investigating the deformation of nanocrystalline copper with microscale kinematic metrics and molecular dynamics. J. Mech. Phys. Solids 60, 471–486.
Zimmerman, J.A., Bammann, D.J., Gao, H., 2009. Deformation gradients for continuum mechanical analysis of atomistic simulations. Int. J. Solids Struct. 46, 238–253.